Geophysical Research Letters

RESEARCH LETTER
10.1029/2024GL108663

Buffering of Aerosol-Cloud Adjustments by Coupling Between Radiative Susceptibility and Precipitation Efficiency

Ci Song[1], Daniel T. McCoy[1], Trude Eidhammer[2], Andrew Gettelman[3], Isabel L. McCoy[4,5], Duncan Watson-Parris[6], Casey J. Wall[7], Gregory Elsaesser[8,9], and Robert Wood[10]

[1]Department of Atmospheric Science, University of Wyoming, Laramie, WY, USA, [2]NSF National Center for Atmospheric Research, Boulder, CO, USA, [3]Pacific Northwest National Laboratory, Richland, WA, USA, [4]Cooperative Institute for Research in Environmental Sciences, University of Colorado, Boulder, CO, USA, [5]Chemical Sciences Laboratory, National Oceanic and Atmospheric Administration, Boulder, CO, USA, [6]Scripps Institution of Oceanography and Halicioğlu Data Science Institute, University of California San Diego, La Jolla, CA, USA, [7]Department of Geosciences, University of Oslo, Oslo, Norway, [8]Columbia University, New York, NY, USA, [9]NASA Goddard Institute for Space Studies, New York, NY, USA, [10]Department of Atmospheric Sciences, University of Washington, Seattle, WA, USA

Abstract Aerosol-cloud interactions (ACI) in warm clouds are the primary source of uncertainty in effective radiative forcing (ERF) during the historical period and, by extension, inferred climate sensitivity. The ERF due to ACI (ERFaci) is composed of the radiative forcing due to changes in cloud microphysics and cloud adjustments to microphysics. Here, we examine the processes that drive ERFaci using a perturbed parameter ensemble (PPE) hosted in CAM6. Observational constraints on the PPE result in substantial constraints in the response of cloud microphysics and macrophysics to anthropogenic aerosol, but only minimal constraint on ERFaci. Examination of cloud and radiation processes in the PPE reveal buffering of ERFaci by the interaction of precipitation efficiency and radiative susceptibility.

Plain Language Summary Uncertainty in predicting future global temperature inferred from the historical record of warming is dominated by how much the warming due to greenhouse gases has been offset by the cooling due to aerosols. Aerosols are small liquid and solid particles that play an important role in cloud formation. The majority of cooling from aerosols is through reflecting incoming solar radiation back to space by cloud. In this study, we constrain an ensemble of possible global model configurations with observations of cloud properties and radiation to reduce uncertainty in the response of clouds and ultimately radiation to anthropogenic aerosol. While observations substantially reduce the uncertainty in both changes in the number of droplets and amount of liquid cloud, the constraint on aerosol cooling is minimal. We argue that the relatively weak constraint is because large changes in cloudiness are accompanied by small change in reflected sunlight due to increased cloudiness.

Key Points:

- Models with lower precipitation efficiency result in larger mean-state liquid water path (LWP) and larger adjustments in LWP to aerosol
- Larger mean-state LWP coincides with lower albedo susceptibility to LWP
- The combination of these processes results in buffering of the radiative effect of LWP adjustments

Supporting Information:

Supporting Information may be found in the online version of this article.

Correspondence to:

C. Song,
csong@uwyo.edu

Citation:

Song, C., McCoy, D. T., Eidhammer, T., Gettelman, A., McCoy, I. L., Watson-Parris, D., et al. (2024). Buffering of aerosol-cloud adjustments by coupling between radiative susceptibility and precipitation efficiency. *Geophysical Research Letters*, *51*, e2024GL108663. https://doi.org/10.1029/2024GL108663

Received 2 FEB 2024
Accepted 30 APR 2024

Author Contributions:

Conceptualization: Daniel T. McCoy
Data curation: Trude Eidhammer, Gregory Elsaesser
Funding acquisition: Daniel T. McCoy
Investigation: Daniel T. McCoy, Trude Eidhammer, Andrew Gettelman, Casey J. Wall
Methodology: Daniel T. McCoy, Trude Eidhammer, Andrew Gettelman, Isabel L. McCoy, Duncan Watson-Parris, Casey J. Wall, Gregory Elsaesser, Robert Wood
Project administration: Daniel T. McCoy
Resources: Duncan Watson-Parris
Software: Duncan Watson-Parris
Supervision: Daniel T. McCoy, Isabel L. McCoy

1. Introduction

Aerosols play an important role in the Earth's energy budget by affecting cloud properties, surface precipitation, and radiation at the top of the atmosphere (Stephens & Ellis, 2008; Twomey, 1991). The change in reflected shortwave radiation from the pre-industrial (PI) to present day (PD) due to anthropogenic perturbations in aerosol is known as aerosol radiative forcing. The radiative forcing from aerosols has larger uncertainty than the radiative forcing from greenhouse gases (GHGs) (Bellouin et al., 2020). The uncertainty in the radiative forcing due to aerosols results in substantial uncertainty in the climate sensitivity to increased greenhouse gases that we can reconcile with the observed temperature record (Andreae et al., 2005; Bellouin et al., 2020; Forster, 2016; Sherwood et al., 2020; Watson-Parris & Smith, 2022; C. Wang, Soden, Yang, & Vecchi, 2021). Longwave radiation is neglected in this study as it has a much smaller effect on aerosol radiative forcing than that from shortwave in warm liquid cloud, but longwave can be important for high altitude, ice-phase cloud (Smith et al., 2020; Zelinka et al., 2014, 2023).

Aerosol-cloud interactions (ACI) in liquid clouds contribute the majority of aerosol forcing (Bellouin et al., 2020). ACI alters the amount of reflected shortwave radiation in liquid cloud in two ways. First, some aerosols serve as cloud condensation nuclei to form cloud droplets. The changes in droplet number concentration

Validation: Duncan Watson-Parris
Writing – original draft: Daniel T. McCoy, Trude Eidhammer, Andrew Gettelman, Isabel L. McCoy, Duncan Watson-Parris, Casey J. Wall, Gregory Elsaesser, Robert Wood
Writing – review & editing: Daniel T. McCoy, Trude Eidhammer, Andrew Gettelman, Isabel L. McCoy, Duncan Watson-Parris, Casey J. Wall, Gregory Elsaesser, Robert Wood

(N_d) from changes in CCN concentration alters the cloud reflectivity even without changes in liquid water content (Twomey, 1977). The change in reflected shortwave radiation is termed instantaneous radiative forcing due to ACI (IRFaci). Second, changes in cloud microphysical processes driven by changes in N_d may alter cloud macrophysical properties (cloud extent in space and time, and the amount of condensate in a cloud) (Ackerman et al., 2004). This is termed the cloud adjustment to aerosol. Process understanding and observations suggest that cloud adjustments could lead to increased or decreased cloud amount and optical thickness (Ackerman et al., 2004; Glassmeier et al., 2021; Toll et al., 2019; Wood, 2007). For example, a reduction in cloud droplet size could lead to the suppression of precipitation and consequently would increase cloud lifetime and condensate mass (Albrecht, 1989). Another example of a potential aerosol-cloud adjustment to increasing N_d is enhanced entrainment of dry air at cloud top due to suppressed precipitation and droplet sedimentation, and more rapid evaporation of smaller droplets. These effects enhance PBL drying and can result in reduced cloud lifetime and condensate mass (Ackerman et al., 2004; Bretherton et al., 2007; S. Wang et al., 2003; Wood, 2007). Given the large number of processes that may be affected, and the causal ambiguity inherent in empirical constraints (Gryspeerdt et al., 2016, 2019; D. T. McCoy et al., 2020; Stevens & Feingold, 2009), it is not surprising that the aggregate effect of aerosol-cloud adjustments on radiative forcing remains highly uncertain (Bellouin et al., 2020). The sum of radiative forcing from IRFaci and aerosol-cloud adjustment is the effective radiatve forcing due to aci (ERFaci).

ERFaci remains poorly constrained by observations, despite the variety of techniques available to observe clouds, radiation, precipitation, and aerosol via surface sites, aircraft, satellites and in the laboratory (Bellouin et al., 2020; Charlson et al., 1992). Here, we examine how ERFaci is constrained by observations of cloud microphysics, macrophysics, and radiation and how processes related to these terms interplay in the prediction of ERFaci.

One possible linear approximation of ERFaci due to liquid clouds is the sum of the response of top of atmosphere (TOA) radiation due to changes in N_d at a fixed cloud macrophysical state and the response of TOA radiation to changes in liquid cloud macrophysical properties induced by changes in N_d (Bellouin et al., 2020; Ghan et al., 2016). This can be expressed mathematically as

$$ERFaci = \left(\frac{\partial R}{\partial \ln N_d}\bigg|_{LWP_c,C} + \frac{\partial R}{\partial C}\frac{dC}{dlnN_d} + \frac{\partial R}{\partial LWP_c}\frac{dLWP_c}{dlnN_d} \right) \cdot \Delta lnN_d \quad (1)$$

where LWP_c is the in-cloud liquid water path (LWP), C is liquid cloud coverage, and ΔlnN_d is the fractional perturbation in N_d (Bellouin et al., 2020; Ghan et al., 2016). The vertical line in the first partial derivative denotes LWP_c and cloud fraction are held constant (Bellouin et al., 2020). While success has been achieved in decomposing model behavior in terms of changes in cloud areal cover and in-cloud liquid water path (Gryspeerdt et al., 2020), there are several limitations that make diagnosing each term from observations and global model output difficult. In practice, liquid condensate mass from GCMs is typically provided as the area-mean ("gridbox mean") rather than in-cloud (Bodas-Salcedo et al., 2011). Passive observations of LWP_c using visible wavelengths in the midlatitudes are difficult due to low sun angles and multilayer cloud (Marchand et al., 2010; Smalley & Lebsock, 2023), in contrast to low-frequency microwave observations of area-mean LWP, which are insensitive to overlying ice cloud (Elsaesser et al., 2017).

In this study, we examine global model behavior in terms of liquid cloud microphysical state (N_d) and aggregated liquid condensate mass (LWP). This follows the approach of previous studies utilizing microphysical state as a constraint on IRFaci (I. L. McCoy et al., 2020) and using LWP as a diagnostic of extratropical liquid cloud variability (D. T. McCoy et al., 2022). We stratify global model-predicted ERFaci in terms of microphysical and macrophysical changes in cloud between PD and PI time periods ($\Delta N_{d(PD-PI)}$ and $\Delta LWP_{(PD-PI)}$). Both quantities are effectively unobservable given the lack of records of the PI state of clouds. One way to constrain these quantities is to use mechanistically motivated relationships between observable and unobservable quantities (Hall & Qu, 2006), but these must be built on process-level understanding (Klein & Hall, 2015). Model simulations can provide the needed observable and unobservable quantities (I. L. McCoy et al., 2020; Regayre et al., 2020). Following on existing literature, we develop constraints on $\Delta N_{d(PD-PI)}$ and $\Delta LWP_{(PD-PI)}$ and, by extension, ERFaci based on observations of clouds and radiation in the present day. The diagnosed impact of these constraints on ERFaci is contextualized using simple models of cloud, precipitation, and radiation processes.

2. Materials and Methods

In this study we examine how cloud, precipitation, aerosol, boundary layer, convective, and radiation processes contribute to ERFaci based on macrophysical and microphysical changes in cloud combined with the effect of cloud on radiation. As discussed in the introduction, many of these processes are parameterized in the global models that we rely on to calculate ERFaci (Smith et al., 2020). To examine this parametric uncertainty and the imprint of these processes on ERFaci, we leverage a perturbed parameter ensemble (PPE) of the Community Atmosphere Model Version 6 (CAM6). The behavior of the CAM6 PPE is contextualized relative to global climate models (GCMs) participating in the sixth Coupled Model Intercomparison Project (CMIP6). Constraints on ERFaci are calculated by confronting the CAM6 PPE with remotely sensed cloud properties and radiative fluxes.

2.1. Simulations

2.1.1. Perturbed Parameter Ensemble

A PPE is an ensemble of simulations with varying parameter combinations conducted in a host model to examine parameter uncertainty (Carslaw et al., 2013; Lee et al., 2011). The CAM6 PPE contains 262 ensemble members each with a unique combination of 45 parameter values (Table S1 in Supporting Information S1). The 45 parameters related to cloud and aerosol processes are simultaneously perturbed using Latin hypercube sampling within an uncertainty range dictated by expert-elicitation. The configuration is fully described in Eidhammer et al. (2024) and Duffy et al. (2023).

For each PPE member, PI and PD aerosol emissions scenarios are integrated for 2 years from 2019 through 2020. Temperature (T) and horizontal wind (U, V) fields are nudged to Modern-Era Retrospective analysis for Research and Applications, Version 2 (MERRA2) reanalysis (Bosilovich et al., 2015). The model configurations are described in detail in Text S1 in Supporting Information S1. The PPE output used in this study is at monthly mean temporal resolution and are described in Table S2 in Supporting Information S1. Cloud top N_d provides a useful diagnostic of model behavior. LWP is available directly as grid-box cloud liquid water path and can be directly compared to microwave radiometer measurements for regions where precipitating liquid contributes less to the total. In addition to outputs related to cloud micro- and macro-physical properties, we examine how clouds affect top of atmosphere radiation. ERFaci is examined and is primarily driven by changes in shortwave radiative flux driven by liquid clouds (Bellouin et al., 2020). Consequently, we examine the sensitivity of all-sky TOA albedo (α) to N_d and LWP. We focus on the ERFaci due to changes in albedo from liquid clouds. A table of variables used to evaluate the microphysical, macrophysical and radiative properties can be found in Table S3 in Supporting Information S1.

To systematically explore parametric uncertainty across the PPE, we build multiple emulators using Gaussian Process (GP) regression (Lee et al., 2011; Watson-Parris et al., 2021). The creation and validation of the emulator is detailed in Text S2 and Figure S2 in Supporting Information S1. We sample the emulator to generate 1,000,000 possible model variants (e.g., parameter combinations) spanning the 45-dimensional parameter space. Those model variants are then compared against observations (Text S2 in Supporting Information S1).

2.1.2. Global Climate Models

Perturbed parameter ensembles provide an evaluation of parametric uncertainty, but say little about structural uncertainty. To evaluate structural uncertainty we compare PPE simulations to several GCMs participating in the sixth Coupled Model Intercomparison Project (CMIP6) (Table S4 in Supporting Information S1). We examine monthly mean output from piClim-aer and piClim-control scenarios. piClim-control set. all emissions to the PI baseline and piClim-aer sets aerosol emission and precursor gases to the present-day and leaves all other emissions at the PI baseline. There is no nudging in these simulations, and 30 years from piClim-aer and piClim-control are used to calculate aerosol forcing (Smith et al., 2020).

The same variables are examined for the PPE and CMIP6 models, although the variable names differ between CAM6 and the CMIP6 labels (Table S5 in Supporting Information S1). The calculation of variables from CMIP6 is fully described in Text S3 in Supporting Information S1.

2.2. Observations

Observations of N_d are derived from the Moderate Resolution Imaging Spectroradiometer (MODIS). N_d is calculated from MODIS retrievals of effective radius (r_e) and optical depth (τ) assuming an adiabatic cloud (D. Grosvenor & Wood, 2014). N_d calculated from MODIS retrievals of cloud properties has been shown to be reasonably un-biased relative to in-situ observations from aircraft (Bennartz & Rausch, 2017; D. P. Grosvenor et al., 2018; Gryspeerdt et al., 2022; Painemal & Zuidema, 2011), although random uncertainty at a pixel-by-pixel level can be large(D. P. Grosvenor et al., 2018). MODIS N_d is calculated for daily means following D. Grosvenor and Wood (2014) for the period 2003–2015 and averaged to 1°. As in I. L. McCoy et al. (2020),the N_d difference between hemispheres is used to constrain the PPE and is calculated as the difference in marine N_d between 30°N to 60°N and 30°S to 60°S ($\Delta N_{d(NH-SH)}$). As in I. L. McCoy et al. (2020), the uncertainty in MODIS $\Delta N_{d(NH-SH)}$ is estimated as the 95% confidence on the interannual range of MODIS $\Delta N_{d(NH-SH)}$.

Observations of LWP are taken from the Multi-Sensor Advanced Climatology of Liquid Water Path (MAC-LWP) for the period 2000–2016 (Elsaesser et al., 2017). The cloud LWP is constructed from 7 sources of satellite microwave data sampling different parts of the diurnal cycle at 0.25° spatial resolution. These samples are aggregated to 1° and provide sampling of LWP throughout the diurnal cycle. Matchups to clear-sky scenes from MODIS are used to reduce cloud LWP bias in cases where clear-sky is observed but non-zero cloud LWP is retrieved due to retrieval cross-talk. MAC-LWP is provided at monthly mean resolution and is only available over ocean. We average MAC-LWP data over global oceanic gridboxes for which rainwater contributes less to mean LWP, since passive microwave radiometers have difficulty distinguishing rainwater from cloudwater (Elsaesser et al., 2017). Gridboxes are only used in the average if the ratio of cloud LWP to total (rain and cloud) LWP exceeds 0.75. Systematic uncertainty in area-weighted mean LWP over the remaining domain is estimated to be less than ±10%,since low frequency passive microwave radiation (used in the retrieval) is more sensitive to integrated liquid mass and minimally sensitive to droplet sizes (Elsaesser et al., 2017). The resulting filtered mask is also applied to the CAM6 PPE and GCM LWP fields for more fair comparison.

We need to quantify the relationship between changes in liquid cloud and changes in top of atmosphere flux to constrain aerosol forcing. We examine clear-sky and all-sky shortwave flux at top of atmosphere contained in the Clouds and the Earth's Radiant Energy System (CERES) Ed 4.1 Energy Balanced And Filled (EBAF) data product for the period 2000–2016 (Loeb et al., 2018). We calculate all-sky and clear-sky TOA albedo (α and α_{clear}) and the susceptibility of α to LWP using CERES α and MAC-LWP over the extratropics (15°N–70°N) (Figure S3 in Supporting Information S1). Given the relatively low uncertainty of around 3% in the observed shortwave TOA CERES fluxes (3 Wm^{-2} relative to an average flux of 98 Wm^{-2}) (Loeb et al., 2018), we assume that the systematic uncertainty associated with the susceptibility of α to LWP is driven by uncertainty in LWP and set to ±10%.

3. Results

Before investigating how ERFaci depends on parameterized processes in the CAM6 PPE, we characterize the prior range of ERFaci. The prior range from the PPE is rather narrow compared to the existing observational prior (Bellouin et al., 2020) and is predicted to be between −2.72 and −1.31 W/m^2 at 95% confidence bounds. This range is based on an emulator trained on the PPE and emulating 1M model variants. Having characterized this prior range, we will examine how ERFaci variability within the PPE is driven by cloud, precipitation, and radiative processes.

3.1. Cloud Microphysical Response

N_d is the key microphysical variable of state setting aerosol-cloud interactions (Wood, 2012). We first examine how the PI to PD change in this quantity ($\Delta N_{d(PD-PI)}$) is constrained by observations.

There is no observational record of PI N_d. Instead, we leverage unperturbed aerosol conditions that occur in the PD as a proxy for the PI state. The pristine Southern Ocean is seen as a good proxy for the PI state as it remains almost unchanged from PI to PD (Hamilton et al., 2014). Overlap between PD and PI N_d is seen across the Southern Hemisphere of the CAM6 PPE (Figure S4 in Supporting Information S1).

Previous studies have used the PD hemispheric contrast in N_d to constrain the anthropogenic perturbation in N_d relative to the PI period (I. L. McCoy et al., 2020). The Northern hemisphere is the region where most aerosol

10.1029/2024GL108663

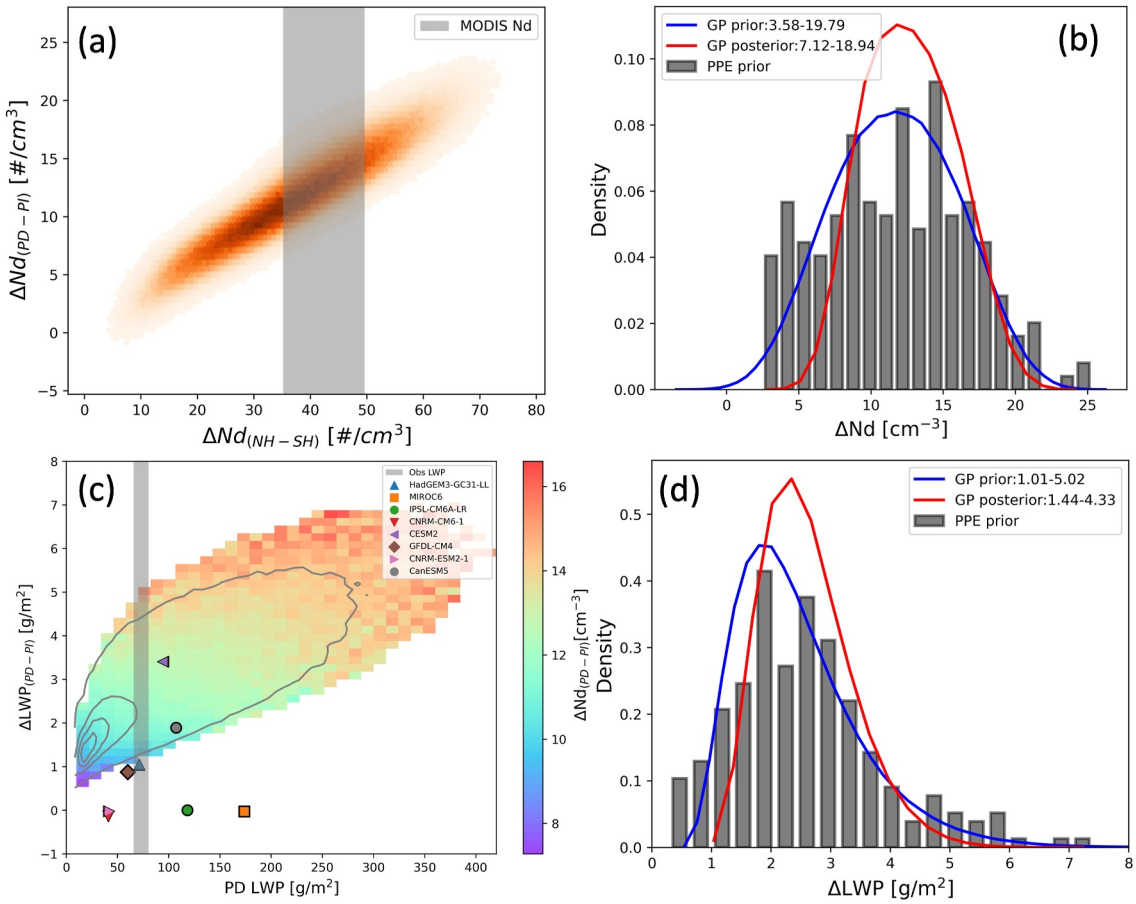

Figure 1. (a)$\Delta N_{d(NH-SH)}$ versus $N_{d(PD-PI)}$ sampled from GP emulators in the CAM6 PPE. Density is shown as orange shading. $\Delta N_{d(NH-SH)}$ is calculated as the difference in annual, area-weighted mean N_d over the ocean between 30°N to 60°N and 30°S to 60°S (averaging boundaries shown as vertical dashed lines in Figure S4 in Supporting Information S1). $\Delta N_{d(PD-PI)}$ is calculated as the global change in oceanic N_d between the PI and PD. MODIS $\Delta N_{d(NH-SH)}$ is shown as the vertical shaded bar. (b) The PDF of $\Delta N_{d(PD-PI)}$ from PPE members (histogram), the GP emulator prior (blue), and observationally constrained posterior (red). (c) Emulated $\Delta LWP_{(PD-PI)}$ versus PD LWP (color shading) and CMIP6 GCMs (color shapes). The color shading shows emulated $\Delta Nd_{(PD-PI)}$ binned by $\Delta LWP_{(PD-PI)}$ and PD LWP. Gray contours indicate the density of emulates. Observed LWP from MAC-LWP for the period 2000–2016 is shown as gray shaded bar on the ordinate. (d) The distribution of $\Delta LWP_{(PD-PI)}$ from the PPE members (histograms), the GP emulator prior (blue line) and the GP posterior constrained by MAC-LWP measurements and N_d from satellite retrievals (red line).

pollution is emitted and it drives the majority of PD-PI change in N_d (Feng & Ramanathan, 2010). We find that the difference in marine N_d between 30°N to 60°N and 30°S to 60°S ($\Delta N_{d(NH-SH)}$) positively correlates with global area-weighted oceanic mean of $\Delta N_{d(PD-PI)}$ from the CAM6 PPE (Figure 1a). This positive correlation is also present in the HadGEM-UKCA PPE (I. L. McCoy et al., 2020; Yoshioka et al., 2019).

MODIS observes $\Delta N_{d(NH-SH)}$ to be between 35 cm^{-3}–49 cm^{-3} assuming 95% interannual uncertainty following previous literature (I. L. McCoy et al., 2020). The uncertainty of N_d from 1 by 1° MODIS retrievals is estimated to be 54% assuming random errors for instrument uncertainty (D. P. Grosvenor et al., 2018). The systematic uncertainty and random uncertainty of hemispheric contrast in N_d is reduced due to three reasons: (a) the random uncertainty in N_d is reduced once it is averaged over 30–60 latitude range over 12 years from 2003 to 2015. (b) the tropics, where N_d calculation is highly unreliable due to high cloud heterogeneity and small cloud fraction in cumulus-dominated regions (D. Grosvenor & Wood, 2014; D. P. Grosvenor et al., 2018; Gryspeerdt et al., 2022), is excluded from our analysis. (c) the difference between hemispheres reduces systematic biases (D. P. Grosvenor et al., 2018; I. L. McCoy et al., 2020). The prior distribution of the change in N_d over global oceans ($\Delta N_{d(PD-PI)}$) from the emulator is 3.58 cm^{-3} to 19.79 cm^{-3} at 95% confidence (Figure 1b). The posterior distribution of $\Delta N_{d(PD-PI)}$, after discarding emulates whose $\Delta N_{d(NH-SH)}$ are inconsistent with MODIS observations, is between 7.12 cm^{-3} and 18.94 cm^{-3} at 95% confidence (Figures 1a and 1b). This equates to a 27% reduction in range and a 8% increase in the median.

The CAM6 PPE explores parametric uncertainty, but does not consider how differences in the underlying model structure may contribute to uncertainty in $\Delta N_{d(PD-PI)}$. It is important to examine multiple GCMs to compare structural differences. I. L. McCoy et al. (2020) examined several Aerocom models as well as a HadGEM-UKCA model PPE. The emergent relationship between hemispheric contrast and PI-PD difference in N_d appeared across these models and the constraint based on the HadGEM-UKCA PPE (8–24 cm^{-3}) is close to the constraint based on the CAM6 PPE. The CMIP6 models examined in this study do not include cloud top N_d outputs, but our agreement with previous work suggests that the hemispheric contrast is robust across model structures. The MODIS N_d is outside of the PPE range in some parts of the 30–60° region used to calculate $\Delta N_{d(NH-SH)}$ (Figure S4 in Supporting Information S1). This is consistent with known biases in the default version of CAM6 (I. L. McCoy et al., 2021; Zhou et al., 2021) and other GCMs (I. L. McCoy et al., 2020) and may reflect missing processes in CAM6 in some regions. However, the $\Delta N_{d(PD-PI)}$ of the CAM6 PPE constrained by the MODIS N_d are similar to the HadGEM-UKCA model PPE (I. L. McCoy et al., 2020) suggesting that despite differing abilities to match the zonal structure of N_d, this constraint is able to effectively constrain $\Delta N_{d(PD-PI)}$.

3.2. Cloud Adjustment

Having examined constraints on $\Delta N_{d(PD-PI)}$, we turn our attention to adjustments in the amount and optical thickness of liquid cloud as characterized by LWP. The response of LWP to increased N_d (e.g., the last term in Equation 1) based on process understanding is uncertain in sign (Bellouin et al., 2020). An important caveat of our analysis is that entrainment feedback to evaporation and sedimentation is not explicitly parameterized in CAM6, similar to other GCMs (D. T. McCoy et al., 2020). Implementation of a drop-size dependent evaporation and entrainment parameterization in a related GCM (CAM5.3-Oslo) did not strongly affect adjustment strength (Karset et al., 2020) and recent surveys of GCMs (including CAM6) find that despite agreeing with observational studies of LWP and Nd inferring size-dependent evaporation and entrainment (Gryspeerdt et al., 2019; Smalley et al., 2024; Zhang & Feingold, 2023), aerosol-cloud adjustments are still dominated by precipitation suppression (Mülmenstädt et al., 2024). Additional analysis is necessary to evaluate the representation of this process in CAM6, and more broadly across GCMs, but is beyond the scope of our study.

A positive correlation is found between changes in area-weighted mean of global oceanic LWP between the PI and PD ($\Delta LWP_{(PD-PI)}$) and area-weighted oceanic mean of PD LWP (Figure 1c). The positive correlation is a direct consequence of precipitation efficiency in liquid clouds. The relationship between N_d, LWP, and precipitation efficiency is shown in Figure S6 in Supporting Information S1. Here, we consider precipitation efficiency in terms of the ability of cloud to generate a given precipitation rate (Li et al., 2022). PPE members with lower precipitation efficiency require a larger LWP to balance condensation and precipitation (Figure S6b in Supporting Information S1), but also create larger adjustments in LWP to changes in N_d (Figure 1c). This can be shown easily based on a simple steady state model of a single-layer cloud balancing condensation, evaporation, and autoconversion-driven precipitation (Jing et al., 2019; Khairoutdinov & Kogan, 2000; Michibata & Takemura, 2015). A step by step derivation is given in Text S4 in Supporting Information S1.

The constraints from MODIS N_d in Section 3.1 have left a subsample of emulates. In this section, we further constrain the subsample by utilizing observed PD LWP to infer the possible range of unobservable $\Delta LWP_{(PD-PI)}$ from this subsample. The posterior distribution of $\Delta LWP_{(PD-PI)}$ is 1.44 g/m^2 to 4.33 g/m^2 at 95% confidence relative to a prior distribution of 1.01 g/m^2 to 5.02 g/m^2 at 95% confidence (Figure 1d). This is a 28% reduction in range and 11% increase in the $\Delta LWP_{(PD-PI)}$ median.

To examine how prevalent the positive correlation between mean state LWP and LWP response to aerosol observed in the PPE is across model structure, we contrast the PPE against CMIP6 GCMs. Several of the CMIP6 GCMs with available model output (Table S4 in Supporting Information S1) agree with the PPE in predicting larger values of $\Delta LWP_{(PD-PI)}$ for larger PD LWP (Figure 1c). This is consistent with the common representation of autoconversion as a power law across GCMs (Jing et al., 2019; Khairoutdinov & Kogan, 2000; Michibata & Takemura, 2015; D. T. McCoy et al., 2020). CESM2 and CanESM5 are well within the PPE spread. GFDL-CM4 and HadGEM3-GC31-LL show relatively smaller change in LWP compared with the CAM6 PPE, but still follow the same general pattern of larger LWP adjustment covarying with larger PD LWP. The remaining GCMs show near-zero change in LWP in response to aerosol. Among those models with near-zero LWP adjustment, CNRM-CM6-1, CNRM-ESM2-1 and IPSL-CM6A-LR only consider first aerosol indirect effect and don't include aerosol-cloud adjustments (Lurton et al., 2020; Michou et al., 2020). We view the behavior of other CMIP6

GCMs as broadly supportive of precipitation efficiency driving relationships between PD LWP and LWP adjustments in GCMs where precipitation-suppression adjustments are permitted in the model physics. When size dependent evaporation and entrainment is explicitly parameterized in model structures, the positive correlation between LWP and $\Delta LWP_{(PD-PI)}$ might be less apparent. However, GCMs with size-dependent evaporation and entrainment parameterized or represented tend to predict $\Delta LWP_{(PD-PI)} > 0$ despite agreeing with observations of size-dependent evaporation and entrainment (Karset et al., 2020; Mülmenstädt et al., 2024). It is difficult to develop a more direct comparison between the GCMs in Figure 1c and the PPE because N_d was not available for all these models.

3.3. Radiative Response

We examined $\Delta N_{d(PD-PI)}$ and $\Delta LWP_{(PD-PI)}$ in Sections 3.1 and 3.2. To constrain aerosol radiative forcing we need to constrain how radiation responds to $\Delta N_{d(PD-PI)}$ and $\Delta LWP_{(PD-PI)}$. At fixed LWP, the susceptibility of α to changes in N_d ($\partial\alpha/\partial N_d$) tells us about how microphysical changes drive IRFaci. Here, we also examine α susceptibility to changes in LWP ($\partial\alpha/\partial$LWP), which tells us about how the radiative effect scales with the magnitude of macrophysical adjustments in liquid condensate.

$\partial\alpha/\partial$LWP is calculated by regressing observations of α on LWP. To minimize the effect of near-horizon solar zenith angles on α (Liou, 2002; D. T. McCoy et al., 2018) we conduct our analysis of α in the summertime (JJA) over open ocean in the Northern Hemisphere (15°N–70°N). $\partial\alpha/\partial$LWP is calculated for PPE members and for the observations (Figure S3 in Supporting Information S1). More details of $\partial\alpha/\partial$LWP calculation can be found in Text S5 in Supporting Information S1.

A negative correlation is found between $\partial\alpha/\partial$LWP and PD LWP across the PPE (Figure 2a). This relationship follows our expectations from radiative transfer as clouds become radiatively saturated with increasing LWP, driving a negative correlation. Because LWP is area mean and not in-cloud, this effect is driven by both saturation in optical depth and in areal coverage (cloud fraction, CF). α scales approximately linearly with cloud area fraction (Bender et al., 2016). α also saturates as in-cloud LWP (LWP_c) increases. This result is consistent with previous work examining CMIP5 and CMIP6 models (D. T. McCoy et al., 2022).

The emergent relationship between LWP and $\partial\alpha/\partial$LWP can be explained using a simple conceptual model assuming conservative scattering. For an overcast region LWP can be written as a function of cloud optical thickness (τ), cloud top effective radius at cloud top (r_e), and water density (ρ_w)

$$LWP = \frac{5}{9}\rho_w \tau r_e \tag{2}$$

Cloud albedo (α_{cld}) can be related to τ assuming conservative scattering equation (Lacis & Hansen, 1974) as

$$\alpha_{cld} \approx \frac{\tau}{\tau + c} \tag{3}$$

where c is a constant. Here, c is set to 7 (Petty, 2006). Combining these equations yields an equation for the dependence of cloudalbedo on LWP for overcast regions

$$\alpha_{cld} \approx \frac{\frac{9}{5}LWP}{\frac{9}{5}LWP + c\rho_w r_e(h)} \tag{4}$$

and all-sky albedos (α) can be calculated for different cloud fractions as

$$\alpha_{=}\alpha_{cld} \cdot CF + (1 - CF) \cdot \alpha_{clear} \tag{5}$$

The cloud fraction of the idealized single-layer cloud is varied from 0.2 to 1.0 and $\alpha_{clear} = 0.1$ over ocean. The predicted dependence of $\partial\alpha/\partial$LWP on mean-state LWP by this simple model qualitatively agrees with the emergent behavior from the CAM6 PPE and CMIP6 GCMs (Figure 2a). The relationship asymptotes to a different value at high LWP because the simplified model shown above only contains a homogeneous and

10.1029/2024GL108663

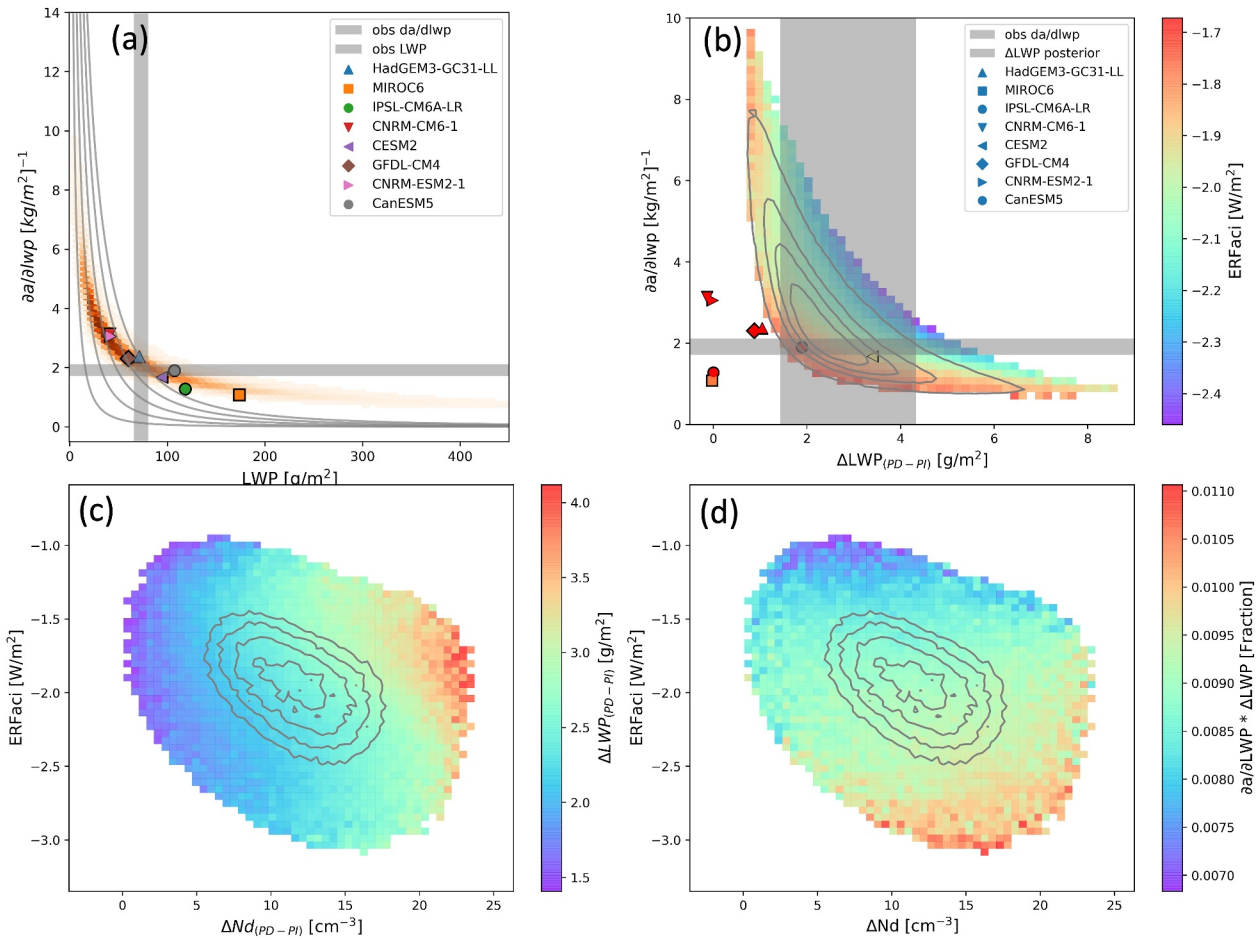

Figure 2. (a) Present day radiative sensitivity to LWP ($\partial\alpha/\partial$LWP) emulated from the PPE (color shading) and from CMIP6 GCMs (color shapes). Emulate density is shown in orange shading. Observations from MAC-LWP are shown as a vertical gray shaded bar and $\partial\alpha/\partial$LWP calculated from MAC-LWP and CERES all-sky TOA albedo (α) is shown as a horizontal gray shaded bar. Calculations from a simple radiative transfer model assuming conservative scattering and fixed cloud fractions from 0.2 (far left) to 1.0 (far right) are shown as gray lines. (b) Emulated $\partial\alpha/\partial$LWP versus $\Delta LWP_{(PD-PI)}$ (color shading) and CMIP6 GCMs (color shapes). Density of emulates is indicated with gray contours. $\partial\alpha/\partial$LWP calculated from MAC-LWP and CERES α is shown as a horizontal gray shaded bar. Constrained $\Delta LWP_{(PD-PI)}$ propagated from (a) is shown as a vertical gray shaded bar. (c) Emulated ERFaci versus $\Delta N_{d(PD-PI)}$ colored by $\Delta LWP_{(PD-PI)}$. (d) Same with (c), but colored by $\Delta LWP_{(PD-PI)}$ scaled byα susceptibility to LWP ($\Delta LWP_{(PD-PI)} \cdot \partial\alpha/\partial LWP$).

radiatively efficient liquid cloud rather than a population of different cloud thicknesses. A more complex radiative model could be created and matched to the PPE behavior, but the physical insight related to α susceptibility provided is the same. CMIP6 GCMs agree with the PPE and we believe the $\partial\alpha/\partial$LWP saturation with LWP is a general behavior across model structures. $\partial\alpha/\partial$LWP calculated from CERES and MAC-LWP also agrees with the PPE in the lower part of Figure 2a.

3.4. Buffering of Adjustment Forcing Due To Precipitation Efficiency and Radiative Susceptibility

We examine ERFaci across the PPE stratified by $\Delta N_{d(PD-PI)}$ and $\Delta LWP_{(PD-PI)}$ (Figure 2c). The IRFaci contribution to ERFaci can be seen in the relationship between $\Delta N_{d(PD-PI)}$ and ERFaci emerging across the PPE. Larger $\Delta N_{d(PD-PI)}$ corresponds to more negative ERFaci, consistent with our expectations (Twomey, 1977). With the narrowed $\Delta N_{d(PD-PI)}$ range constrained by MODIS N_d in Section 3.1, ERFaci is estimated to be between -2.72 W/m^2 to -1.31 W/m^2 at 95% confidence bounds (Figure 3a). The ERFaci range shifts to more negative values with $\Delta N_{d(PD-PI)}$ constrained to larger values, consistent with Twomey effect.

We expect a larger change in LWP would also lead to stronger aerosol cooling as the increased cloud thickness and cloud coverage would reflect more shortwave radiation back to space, resulting in a cooling effect. However, larger $\Delta LWP_{(PD-PI)}$ does not correspond to stronger ERFaci in the PPE (Figure 2c). There is a weak relationship

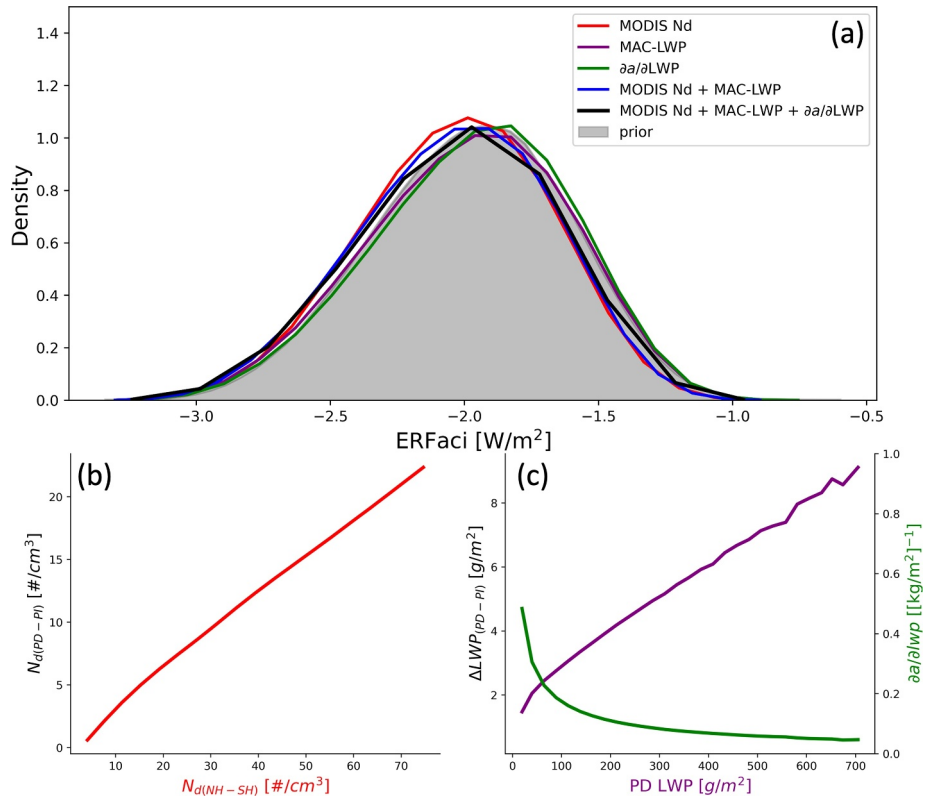

Figure 3. (a) The distribution of emulated ERFaci prior (gray shading), and observationally constrained posterior at their 95% confidence intervals from MODIS N_d only (red), MAC-LWP only (purple), calculated $d\alpha$/dLWP only from CERES radiative fluxes and MAC-LWP (green), MODIS N_d and MAC-LWP (blue), and the posterior from all three lines of observational constraints (black). (b) Changes in oceanic N_d between the PI and PD ($\Delta N_{d(PD-PI)}$) and hemispheric contrast in N_d ($\Delta N_{d(NH-SH)}$) positively correlate across CAM6 PPE. (c) Radiative sensitivity ($\partial\alpha/\partial$LWP) and $\Delta LWP_{(PD-PI)}$ anticorrelate across CAM6 PPE as a function of mean-state LWP (PD LWP)).

between $\Delta LWP_{(PD-PI)}$ at lower $\Delta N_{d(PD-PI)}$ (<10 cm^{-3}). At higher $\Delta N_{d(PD-PI)}$ (>10 cm^{-3}), larger $\Delta LWP_{(PD-PI)}$ correlates with weaker ERFaci. The result is the opposite from what has been found by Zhao et al. (2024). In Zhao et al. (2024), cloud physics parameters that are important to ice processes are perturbed. Models with weaker ice production processes tend to simulate more LWP as well as stronger (more negative) ERFaci. This is because ice clouds are optically thinner and reflect less solar radiation back to space than liquid water clouds (Lohmann, 2017). In the CAM6 PPE, in addition to perturbing ice processes, liquid processes, convection, and aerosol processes that are important to ACI are also perturbed (Table S1 in Supporting Information S1). We find that parameters associated with rain processes (Khairoutdinov & Kogan, 2000) dominate the cloud liquid amount in liquid cloud, while in Zhao et al. (2024) the mean-state LWP in mix-phase cloud is driven by perturbations to ice processes.

Constraining $\Delta LWP_{(PD-PI)}$ based on MAC-LWP (Section 3.2) does not change the estimated ERFaci range from its prior distribution (Figure 3a). By combining the constraints from $\Delta N_{d(PD-PI)}$ and $\Delta LWP_{(PD-PI)}$, ERFaci is estimated to be between −2.77 W/m^2 to −1.39 W/m^2 at 95% confidence bounds, which equates to 2% reduction in range compared to the prior distribution (Figure 3a). This small reduction in range is surprising given the large potential contribution of aerosol-cloud adjustments to enhancing ERFaci (Bellouin et al., 2020).

Larger $\Delta LWP_{(PD-PI)}$ does not correspond to stronger ERFaci because of compensation by lower $\partial\alpha/\partial$LWP (Figure 2b). Larger $\Delta LWP_{(PD-PI)}$ is accompanied with lower $\partial\alpha/\partial$LWP due to (a) the underlying negative correlation between $\partial\alpha/\partial$LWP and PD LWP (Figure 2a) driven by radiative saturation and (b) the positive correlation between $\Delta LWP_{(PD-PI)}$ and PD LWP (Figure 1c) driven by precipitation efficiency (Figure S6 in Supporting Information S1), which results in a negative correlation between $\Delta LWP_{(PD-PI)}$ and $\partial\alpha/\partial$LWP (Figure 2b). As a result, more negative ERFaci is expected with a larger change in $\Delta N_{d(PD-PI)}$ while ERFaci is relatively insensitive

to $\Delta LWP_{(PD-PI)}$ due to the buffering between LWP adjustments ($\Delta LWP_{(PD-PI)}$) and radiative sensitivity to LWP ($\partial\alpha/\partial$LWP) driven by precipitation efficiency and radiative saturation. This effect also appears to manifest itself in the prior distribution of ERFaci in the PPE, which is relatively narrow (Figure 3a: -2.72 W/m^2 to -1.31 W/m^2 at 95% confidence) and is in fact narrower than the expert-predicted range in Bellouin et al. (2020). Parameter combinations do exist where ERFaci can be relatively strong when both $\partial\alpha/\partial$LWP and $\Delta LWP_{(PD-PI)}$ are large (Figure 2b). When this compensating effect is accounted for and $\Delta LWP_{(PD-PI)}$ is scaled by $\partial\alpha/\partial$LWP, then a dependence of ERFaci on adjustments emerges (Figure 2d). We thus add $\partial\alpha/\partial$LWP as another constraint on ERFaci. However, the ERFaci constraint is still minimal when adding $\partial\alpha/\partial$LWP as an observational constraint (Figure 3a). This is because the range of $\Delta LWP_{(PD-PI)}$ is wide and therefore the scaled $\Delta LWP_{(PD-PI)}$ by α susceptibility ($\partial\alpha/\partial$LWP * $\Delta LWP_{(PD-PI)}$) is too wide to provide a tight constraint on ERFaci (Figure 2b). If a narrower range of $\Delta LWP_{(PD-PI)}$ can be achieved with more accurate LWP measurements, we would expect a tighter of ERFaci constraints.

We compare CMIP6 GCMs with the CAM6 PPE to investigate whether this buffering effect can be seen across model structures. Except for CESM2 and CanESM5, none of the CMIP6 GCMs are consistent with the CAM6 PPE. The buffering between LWP adjustment and radiative sensitivity to LWP might be specific to the CAM6 model setup but similar buffering may occur around the default configuration of each GCM. The number of GCMs with the necessary data to perform this analysis and that permit liquid cloud adjustments is small-making it difficult to systematically explore this behavior in the same way that we are able to in CAM6 using the PPE approach.

As discussed in Section 3.2, the sedimentation-evaporation feedback might possibly alter the positive correlation between PD LWP and $\Delta LWP_{(PD-PI)}$ in the CAM6 PPE through depleting cloud liquid water. The buffering effect might be suppressed when the sedimentation-evaporation feedback is included in the CAM6 PPE.

4. Conclusions

In this work we probe how different parameterized processes interact and imprint on the effective radiative forcing due to aersol-cloud interactions (ERFaci). In our analysis we utilize remote sensing observations to constrain ERFaci. We apply a sequence of constraints designed to target processes contributing to ERFaci (Equation 1).

Hemispheric contrast in N_d is utilized to constrain the PI to PD change in N_d. Based on the satellite-derived $\Delta N_{d(NH-SH)}$ and the positive correlation between $\Delta N_{d(NH-SH)}$ and $\Delta N_{d(PD-PI)}$ from the CAM6 PPE (Figure 3b), the global area-weighted oceanic $\Delta N_{d(PD-PI)}$ is constrained to be between 7.12 cm^{-3} and 18.94 cm^{-3} at 95% confidence. This range is reduced by 27% (from 3.58 cm^{-3}–19.79 cm^{-3} at 95% confidence) and the median shifts from 11.68 cm^{-3}–12.60 cm^{-3} (Figure 1b) and is consistent with previous studies (I. L. McCoy et al., 2020).

We combine microwave radiometer remote sensing of LWP with satellite retrievals of N_d to constrain aerosol-cloud adjustments in liquid cloud. The range of constrained $\Delta LWP_{(PD-PI)}$ decreases 28% (1.01 g/m^2 to 5.02 g/m^2 decreases to 1.44 g/m^2 to 4.33 g/m^2). The median increases 11% from 2.25 to 2.50 g/m^2 (Figure 1d).

Finally, we examine the $\partial\alpha/\partial$LWP as a constraint on ERFaci. We find that albedo susceptibility across the PPE and CMIP6 GCMs is strongly dependent on mean-state LWP (Figure 2a). ERFaci is constrained by combining all lines of observations. The range of global, annual mean ERFaci is reduced by 2% (-2.72 W/m^2 to -1.31 W/m^2 decreases to -2.76 W/m^2 to -1.38 W/m^2). The median shifts from -1.97 W/m^2 to -2.01 W/m^2 (Figure 3a).

The constraint on global annual mean ERFaci (2% reduction in range and 2% decease in median) is relatively small compared to the constraints on $\Delta N_{d(PD-PI)}$ (27% reduction in range and 8% increase in median), and $\Delta LWP_{(PD-PI)}$ (28% increase in range and 11% increase in median) developed in our study. We argue that the relative scale of this constraint is due to interactions between precipitation efficiency and radiative susceptibility to LWP. PPE members with lower precipitation efficiency tend to have higher LWP in the mean state(Figure S6b in Supporting Information S1) as well as larger LWP adjustments to aerosols (Figure 1c). High LWP in these PPE members also results in the members being closer to radiative saturation and having a weaker radiative response to changes in LWP (Figure 3c). The interplay of these processes results in a washing out of the radiative effect from liquid cloud adjustments due to the buffering of the radiative effect by reduced radiative sensitivity. Because of this buffering effect, the prior range of the CAM6 PPE ERFaci is narrower compared with the estimate from Bellouin et al. (2020). The underlying processes driving this buffering are not particularly unique to CAM6 and

may manifest itself in other GCMs where precipitation suppression is parameterized. Consideration of this effect may prove useful for GCM development efforts and in understanding the representation of historical aerosol cooling in GCMs.

Data Availability Statement

Cloud droplet number concentration from MODIS is available at online in NetCDF format from the Centre for European Data Analysis (CEDA) (D. Grosvenor & Wood, 2018). MAC-LWP is available through the Goddard Earth Sciences Data and Information Services Center (GES DISC, current hosting: http://disc.sci.gsfc.nasa.gov) Radiative fluxes from CERES is available through the CERES subsetting tool (CERES EBAF Ed4.2, 2023). CMIP6 data is available through the Earth System Grid Federation (CMIP6 Earth System Grid Federation, 2023). PPE output is available online (Eidhammer, 2023).

Acknowledgments
We would like to acknowledge the use of computational resources (https://doi.org/10.5065/D6RX99HX) at the NCAR-Wyoming Supercomputing Center provided by the National Science Foundation and the State of Wyoming, and supported by NCAR's Computational and Information Systems Laboratory. ILM was supported by NOAA cooperative agreements NA17OAR4320101 and NA22OAR4320151. CJW received funding from the European Union's Horizon 2020 research and innovation programme under the Marie Skłodowska-Curie grant agreement No. 101019911. CS and DTM were supported by NASA Grant 80NSSC21K2014 and DTM was supported by the U.S. Department of Energy's Atmospheric System Research Federal Award DE-SC002227 and U.S. Department of Energy's Established Program to Stimulate Competitive Research DE-SC0024161. GSE acknowledges support from the NSF STC Learning the Earth with Artificial Intelligence and Physics (LEAP), NSF Award Number 2019625.

References

Ackerman, A. S., Kirkpatrick, M. P., Stevens, D. E., & Toon, O. B. (2004). The impact of humidity above stratiform clouds on indirect aerosol climate forcing. *Nature*, *432*(7020), 1014–1017. https://doi.org/10.1038/nature03174

Albrecht, B. A. (1989). Aerosols, cloud microphysics, and fractional cloudiness. *Science*, *245*(4923), 1227–1230. https://doi.org/10.1126/science.245.4923.1227

Andreae, M. O., Jones, C. D., & Cox, P. M. (2005). Strong present-day aerosol cooling implies a hot future. *Nature*, *435*(7046), 1187–1190. https://doi.org/10.1038/nature03671

Bellouin, N., Quaas, J., Gryspeerdt, E., Kinne, S., Stier, P., Watson-Parris, D., et al. (2020). Bounding global aerosol radiative forcing of climate change. *Reviews of Geophysics*, *58*(1), e2019RG000660. https://doi.org/10.1029/2019rg000660

Bender, F. A.-M., Engström, A., & Karlsson, J. (2016). Factors controlling cloud albedo in marine subtropical stratocumulus regions in climate models and satellite observations. *Journal of Climate*, *29*(10), 3559–3587. https://doi.org/10.1175/jcli-d-15-0095.1

Bennartz, R., & Rausch, J. (2017). Global and regional estimates of warm cloud droplet number concentration based on 13 years of AQUA-MODIS observations. *Atmospheric Chemistry and Physics*, *17*(16), 9815–9836. https://doi.org/10.5194/acp-17-9815-2017

Bodas-Salcedo, A., Webb, M. J., Bony, S., Chepfer, H., Dufresne, J.-L., Klein, S. A., et al. (2011). COSP: Satellite simulation software for model assessment. *Bulletin of the American Meteorological Society*, *92*(8), 1023–1043. https://doi.org/10.1175/2011BAMS2856.1

Bosilovich, M., Akella, S., Coy, L., Cullather, R., Draper, C., Gelaro, R., et al. (2015). *Technical report series on global modeling and data assimilation, volume 43 MERRA-2: Initial evaluation of the climate*. NASA-GMAO. Retrieved from https://gmao.gsfc.nasa.gov/pubs/docs/Bosilovich803.pdf

Bretherton, C., Blossey, P. N., & Uchida, J. (2007). Cloud droplet sedimentation, entrainment efficiency, and subtropical stratocumulus albedo. *Geophysical Research Letters*, *34*(3), L03813. https://doi.org/10.1029/2006gl027648

Carslaw, K., Lee, L., Reddington, C., Pringle, K., Rap, A., Forster, P., et al. (2013). Large contribution of natural aerosols to uncertainty in indirect forcing. *Nature*, *503*(7474), 67–71. https://doi.org/10.1038/nature12674

CERES EBAF ED4.2. (2023). CERES EBAF ED4.2 [Dataset]. *CERES*. Retrieved from https://ceres.larc.nasa.gov/documents/DQ_summaries/CERES_EBAF_Ed4.2_DQS.pdf

Charlson, R. J., Schwartz, S., Hales, J., Cess, R. D., Coakley Jr, J., Hansen, J., & Hofmann, D. (1992). Climate forcing by anthropogenic aerosols. *Science*, *255*(5043), 423–430. https://doi.org/10.1126/science.255.5043.423

CMIP6 Earth system grid federation. (2023). CMIP6 Earth system grid federation. [Dataset]. *GMD*. https://doi.org/10.5194/gmd-9-3447-2016

Duffy, M. L., Medeiros, B., Gettelman, A., & Eidhammer, T. (2023). Perturbing parameters to understand cloud contributions to climate change. *Journal of Climate*, *37*(1), 213–227. https://doi.org/10.1175/jcli-d-23-0250.1

Eidhammer, T. (2023). CESM2.2 PPE [Dataset]. *NCAR*. https://doi.org/10.26024/bzne-yf09

Eidhammer, T., Gettelman, A., Thayer-Calder, K., Watson-Parris, D., Morrison, H., van Lier-Walqui, M., et al. (2024). An extensible perturbed parameter ensemble (PPE) for the community atmosphere model version 6. *Geoscientific Model Development*, *16*, 1735–1754. https://doi.org/10.5194/gmd-17-7835-2024

Elsaesser, G. S., O'Dell, C. W., Lebsock, M. D., Bennartz, R., Greenwald, T. J., & Wentz, F. J. (2017). The multisensor advanced climatology of liquid water path (MAC-LWP). *Journal of Climate*, *30*(24), 10193–10210. https://doi.org/10.1175/jcli-d-16-0902.1

Feng, Y., & Ramanathan, V. (2010). Investigation of aerosol–cloud interactions using a chemical transport model constrained by satellite observations. *Tellus B: Chemical and Physical Meteorology*, *62*(1), 69–86. https://doi.org/10.1111/j.1600-0889.2009.00444.x

Forster, P. M. (2016). Inference of climate sensitivity from analysis of Earth's energy budget. *Annual Review of Earth and Planetary Sciences*, *44*(1), 85–106. https://doi.org/10.1146/annurev-earth-060614-105156

Ghan, S., Wang, M., Zhang, S., Ferrachat, S., Gettelman, A., Griesfeller, J., et al. (2016). Challenges in constraining anthropogenic aerosol effects on cloud radiative forcing using present-day spatiotemporal variability. *Proceedings of the National Academy of Sciences of the United States of America*, *113*(21), 5804–5811. https://doi.org/10.1073/pnas.1514036113

Glassmeier, F., Hoffmann, F., Johnson, J. S., Yamaguchi, T., Carslaw, K. S., & Feingold, G. (2021). Aerosol-cloud-climate cooling overestimated by ship-track data. *Science*, *371*(6528), 485–489. https://doi.org/10.1126/science.abd3980

Grosvenor, D., & Wood, R. (2014). The effect of solar zenith angle on MODIS cloud optical and microphysical retrievals within marine liquid water clouds. *Atmospheric Chemistry and Physics*, *14*(14), 7291–7321. https://doi.org/10.5194/acp-14-7291-2014

Grosvenor, D., & Wood, R. (2018). MODIS cloud droplet number concentration [Dataset]. *CEDA*. Retrieved from https://catalogue.ceda.ac.uk/uuid/cf97ccc802d348ec8a3b6f2995dfbbff

Grosvenor, D. P., Sourdeval, O., Zuidema, P., Ackerman, A., Alexandrov, M. D., Bennartz, R., et al. (2018). Remote sensing of droplet number concentration in warm clouds: A review of the current state of knowledge and perspectives. *Reviews of Geophysics*, *56*(2), 409–453. https://doi.org/10.1029/2017RG000593

Gryspeerdt, E., Goren, T., Sourdeval, O., Quaas, J., Mülmenstädt, J., Dipu, S., et al. (2019). Constraining the aerosol influence on cloud liquid water path. *Atmospheric Chemistry and Physics*, *19*(8), 5331–5347. https://doi.org/10.5194/acp-19-5331-2019

Gryspeerdt, E., McCoy, D. T., Crosbie, E., Moore, R. H., Nott, G. J., Painemal, D., et al. (2022). The impact of sampling strategy on the cloud droplet number concentration estimated from satellite data. *Atmospheric Measurement Techniques*, *15*(12), 3875–3892. https://doi.org/10.5194/amt-15-3875-2022

Gryspeerdt, E., Mülmenstädt, J., Gettelman, A., Malavelle, F. F., Morrison, H., Neubauer, D., et al. (2020). Surprising similarities in model and observational aerosol radiative forcing estimates. *Atmospheric Chemistry and Physics*, *20*(1), 613–623. https://doi.org/10.5194/acp-20-613-2020

Gryspeerdt, E., Quaas, J., & Bellouin, N. (2016). Constraining the aerosol influence on cloud fraction. *Journal of Geophysical Research: Atmospheres*, *121*(7), 3566–3583. https://doi.org/10.1002/2015jd023744

Hall, A., & Qu, X. (2006). Using the current seasonal cycle to constrain snow albedo feedback in future climate change. *Geophysical Research Letters*, *33*(3), L03502. https://doi.org/10.1029/2005gl025127

Hamilton, D. S., Lee, L. A., Pringle, K. J., Reddington, C. L., Spracklen, D. V., & Carslaw, K. S. (2014). Occurrence of pristine aerosol environments on a polluted planet. *Proceedings of the National Academy of Sciences of the United States of America*, *111*(52), 18466–18471. https://doi.org/10.1073/pnas.1415440111

Jing, X., Suzuki, K., & Michibata, T. (2019). The key role of warm rain parameterization in determining the aerosol indirect effect in a global climate model. *Journal of Climate*, *32*(14), 4409–4430. https://doi.org/10.1175/jcli-d-18-0789.1

Karset, I. H. H., Gettelman, A., Storelvmo, T., Alterskjær, K., & Berntsen, T. K. (2020). Exploring impacts of size-dependent evaporation and entrainment in a global model. *Journal of Geophysical Research: Atmospheres*, *125*(4), e2019JD031817. https://doi.org/10.1029/2019jd031817

Khairoutdinov, M., & Kogan, Y. (2000). A new cloud physics parameterization in a large-eddy simulation model of marine stratocumulus. *Monthly Weather Review*, *128*(1), 229–243. https://doi.org/10.1175/1520-0493(2000)128<0229:ancppi>2.0.co;2

Klein, S. A., & Hall, A. (2015). Emergent constraints for cloud feedbacks. *Current Climate Change Reports*, *1*(4), 276–287. https://doi.org/10.1007/s40641-015-0027-1

Lacis, A. A., & Hansen, J. (1974). A parameterization for the absorption of solar radiation in the earth's atmosphere. *Journal of the Atmospheric Sciences*, *31*(1), 118–133. https://doi.org/10.1175/1520-0469(1974)031<0118:apftao>2.0.co;2

Lee, L., Carslaw, K., Pringle, K., Mann, G., & Spracklen, D. (2011). Emulation of a complex global aerosol model to quantify sensitivity to uncertain parameters. *Atmospheric Chemistry and Physics*, *11*(23), 12253–12273. https://doi.org/10.5194/acp-11-12253-2011

Li, R. L., Studholme, J. H., Fedorov, A. V., & Storelvmo, T. (2022). Precipitation efficiency constraint on climate change. *Nature Climate Change*, *12*(7), 642–648. https://doi.org/10.1038/s41558-022-01400-x

Liou, K.-N. (2002). An introduction to atmospheric radiation. In *International geophysics* (Vol. 84). Elsevier. https://doi.org/10.1016/s0074-6142(02)x8015-2

Loeb, N. G., Doelling, D. R., Wang, H., Su, W., Nguyen, C., Corbett, J. G., et al. (2018). Clouds and the earth's radiant energy system (CERES) energy balanced and filled (EBAF) top-of-atmosphere (TOA) edition-4.0 data product. *Journal of Climate*, *31*(2), 895–918. https://doi.org/10.1175/jcli-d-17-0208.1

Lohmann, U. (2017). Anthropogenic aerosol influences on mixed-phase clouds. *Current Climate Change Reports*, *3*(1), 32–44. https://doi.org/10.1007/s40641-017-0059-9

Lurton, T., Balkanski, Y., Bastrikov, V., Bekki, S., Bopp, L., Braconnot, P., et al. (2020). Implementation of the CMIP6 forcing data in the IPSL-CM6A-LR model. *Journal of Advances in Modeling Earth Systems*, *12*(4), e2019MS001940. https://doi.org/10.1029/2019ms001940

Marchand, R., Ackerman, T., Smyth, M., & Rossow, W. B. (2010). A review of cloud top height and optical depth histograms from MISR, ISCCP, and MODIS. *Journal of Geophysical Research*, *115*(D16), D16206. https://doi.org/10.1029/2009jd013422

McCoy, D. T., Field, P., Frazer, M. E., Zelinka, M. D., Elsaesser, G. S., Mülmenstädt, J., et al. (2022). Extratropical shortwave cloud feedbacks in the context of the global circulation and hydrological cycle. *Geophysical Research Letters*, *49*(8), e2021GL097154. https://doi.org/10.1029/2021gl097154

McCoy, D. T., Field, P., Gordon, H., Elsaesser, G. S., & Grosvenor, D. P. (2020). Untangling causality in midlatitude aerosol–cloud adjustments. *Atmospheric Chemistry and Physics*, *20*(7), 4085–4103. https://doi.org/10.5194/acp-20-4085-2020

McCoy, D. T., Field, P. R., Schmidt, A., Grosvenor, D. P., Bender, F. A.-M., Shipway, B. J., et al. (2018). Aerosol midlatitude cyclone indirect effects in observations and high-resolution simulations. *Atmospheric Chemistry and Physics*, *18*(8), 5821–5846. https://doi.org/10.5194/acp-18-5821-2018

McCoy, I. L., Bretherton, C. S., Wood, R., Twohy, C. H., Gettelman, A., Bardeen, C. G., & Toohey, D. W. (2021). Influences of recent particle formation on southern ocean aerosol variability and low cloud properties. *Journal of Geophysical Research: Atmospheres*, *126*(8), e2020JD033529. https://doi.org/10.1029/2020jd033529

McCoy, I. L., McCoy, D. T., Wood, R., Regayre, L., Watson-Parris, D., Grosvenor, D. P., et al. (2020). The hemispheric contrast in cloud microphysical properties constrains aerosol forcing. *Proceedings of the National Academy of Sciences of the United States of America*, *117*(32), 18998–19006. https://doi.org/10.1073/pnas.1922502117

Michibata, T., & Takemura, T. (2015). Evaluation of autoconversion schemes in a single model framework with satellite observations. *Journal of Geophysical Research: Atmospheres*, *120*(18), 9570–9590. https://doi.org/10.1002/2015jd023818-t

Michou, M., Nabat, P., Saint-Martin, D., Bock, J., Decharme, B., Mallet, M., et al. (2020). Present-day and historical aerosol and ozone characteristics in CNRM CMIP6 simulations. *Journal of Advances in Modeling Earth Systems*, *12*(1), e2019MS001816. https://doi.org/10.1029/2019ms001816

Mülmenstädt, J., Gryspeerdt, E., Dipu, S., Quaas, J., Ackerman, A. S., Fridlind, A. M., et al. (2024). General circulation models simulate negative liquid water path–droplet number correlations, but anthropogenic aerosols still increase simulated liquid water path. *EGUsphere*, 1–29.

Painemal, D., & Zuidema, P. (2011). Assessment of MODIS cloud effective radius and optical thickness retrievals over the southeast pacific with vocals-rex in situ measurements. *Journal of Geophysical Research*, *116*(D24), D24206. https://doi.org/10.1029/2011JD016155

Petty, G. (2006). *A first course in atmospheric radiation*. Sundog Pub. Retrieved from https://books.google.com/books?id=YpspAQAAMAAJ

Regayre, L. A., Schmale, J., Johnson, J. S., Tatzelt, C., Baccarini, A., Henning, S., et al. (2020). The value of remote marine aerosol measurements for constraining radiative forcing uncertainty. *Atmospheric Chemistry and Physics*, *20*(16), 10063–10072. https://doi.org/10.5194/acp-20-10063-2020

Sherwood, S. C., Webb, M. J., Annan, J. D., Armour, K. C., Forster, P. M., Hargreaves, J. C., et al. (2020). An assessment of Earth's climate sensitivity using multiple lines of evidence. *Reviews of Geophysics*, *58*(4), e2019RG000678. https://doi.org/10.1029/2019rg000678

Smalley, K. M., & Lebsock, M. D. (2023). Corrections for geostationary cloud liquid water path using microwave imagery. *Journal of Atmospheric and Oceanic Technology*, *40*(9), 1049–1061. https://doi.org/10.1175/jtech-d-23-0030.1

Smalley, K. M., Lebsock, M. D., & Eastman, R. (2024). Diurnal patterns in the observed cloud liquid water path response to droplet number perturbations. *Geophysical Research Letters*, *51*(4), e2023GL107323. https://doi.org/10.1029/2023gl107323

Smith, C. J., Kramer, R. J., Myhre, G., Alterskjær, K., Collins, W., Sima, A., et al. (2020). Effective radiative forcing and adjustments in CMIP6 models. *Atmospheric Chemistry and Physics*, *20*(16), 9591–9618. https://doi.org/10.5194/acp-20-9591-2020

Stephens, G. L., & Ellis, T. D. (2008). Controls of global-mean precipitation increases in global warming GCM experiments. *Journal of Climate*, *21*(23), 6141–6155. https://doi.org/10.1175/2008jcli2144.1

Stevens, B., & Feingold, G. (2009). Untangling aerosol effects on clouds and precipitation in a buffered system. *Nature*, *461*(7264), 607–613. https://doi.org/10.1038/nature08281

Toll, V., Christensen, M., Quaas, J., & Bellouin, N. (2019). Weak average liquid-cloud-water response to anthropogenic aerosols. *Nature*, *572*(7767), 51–55. https://doi.org/10.1038/s41586-019-1423-9

Twomey, S. (1977). The influence of pollution on the shortwave albedo of clouds. *Journal of the Atmospheric Sciences*, *34*(7), 1149–1152. https://doi.org/10.1175/1520-0469(1977)034<1149:tiopot>2.0.co;2

Twomey, S. (1991). Aerosols, clouds and radiation. *Atmospheric Environment. Part A. General Topics*, *25*(11), 2435–2442. https://doi.org/10.1016/0960-1686(91)90159-5

Wang, C., Soden, B. J., Yang, W., & Vecchi, G. A. (2021). Compensation between cloud feedback and aerosol-cloud interaction in CMIP6 models. *Geophysical Research Letters*, *48*(4), e2020GL091024. https://doi.org/10.1029/2020gl091024

Wang, S., Wang, Q., & Feingold, G. (2003). Turbulence, condensation, and liquid water transport in numerically simulated nonprecipitating stratocumulus clouds. *Journal of the Atmospheric Sciences*, *60*(2), 262–278. https://doi.org/10.1175/1520-0469(2003)060<0262:tcalwt>2.0.co;2

Watson-Parris, D., & Smith, C. J. (2022). Large uncertainty in future warming due to aerosol forcing. *Nature Climate Change*, *12*(12), 1111–1113. https://doi.org/10.1038/s41558-022-01516-0

Watson-Parris, D., Williams, A., Deaconu, L., & Stier, P. (2021). Model calibration using ESEM v1. 1.0–an open, scalable Earth system emulator. *Geoscientific Model Development*, *14*(12), 7659–7672. https://doi.org/10.5194/gmd-14-7659-2021

Wood, R. (2007). Cancellation of aerosol indirect effects in marine stratocumulus through cloud thinning. *Journal of the Atmospheric Sciences*, *64*(7), 2657–2669. https://doi.org/10.1175/jas3942.1

Wood, R. (2012). Stratocumulus clouds. *Monthly Weather Review*, *140*(8), 2373–2423. https://doi.org/10.1175/mwr-d-11-00121.1

Yoshioka, M., Regayre, L., Pringle, K., Johnson, J., Mann, G., Partridge, D., et al. (2019). Ensembles of global climate model variants designed for the quantification and constraint of uncertainty in aerosols and their radiative forcing. *Journal of Advances in Modeling Earth Systems*, *11*(11), 3728–3754. https://doi.org/10.1029/2019ms001628

Zelinka, M. D., Andrews, T., Forster, P. M., & Taylor, K. E. (2014). Quantifying components of aerosol-cloud-radiation interactions in climate models. *Journal of Geophysical Research: Atmospheres*, *119*(12), 7599–7615. https://doi.org/10.1002/2014jd021710

Zelinka, M. D., Smith, C. J., Qin, Y., & Taylor, K. E. (2023). Comparison of methods to estimate aerosol effective radiative forcings in climate models. *Atmospheric Chemistry and Physics*, *23*(15), 8879–8898. https://doi.org/10.5194/acp-23-8879-2023

Zhang, J., & Feingold, G. (2023). Distinct regional meteorological influences on low-cloud albedo susceptibility over global marine stratocumulus regions. *Atmospheric Chemistry and Physics*, *23*(2), 1073–1090. https://doi.org/10.5194/acp-23-1073-2023

Zhao, X., Liu, X., Lin, L., Qin, Y., Zelinka, M. D., Klein, S. A., et al. (2024). Larger cloud liquid water enhances both aerosol indirect forcing and cloud radiative feedback in two earth system models. *Geophysical Research Letters*, *51*(2), e2023GL105529. https://doi.org/10.1029/2023gl105529

Zhou, X., Atlas, R., McCoy, I. L., Bretherton, C. S., Bardeen, C., Gettelman, A., et al. (2021). Evaluation of cloud and precipitation simulations in CAM6 and AM4 using observations over the southern ocean. *Earth and Space Science*, *8*(2), e2020EA001241. https://doi.org/10.1029/2020ea001241